frontiers | Frontiers in Geochemistry

TYPE Original Research
PUBLISHED 15 August 2025
DOI 10.3389/fgeoc.2025.1607472

OPEN ACCESS

EDITED BY
Michael Roden,
University of Georgia, United States

REVIEWED BY
Abdel-Aal M. Abdel-Karim,
Zagazig University, Egypt
Izaac Cabral Neto,
Geological Survey of Brazil, Brazil

*CORRESPONDENCE
V. Stagno,
vincenzo.stagno@uniroma1.it
G. Marras,
giulia.marras@uniroma1.it

RECEIVED 07 April 2025
ACCEPTED 17 July 2025
PUBLISHED 15 August 2025

CITATION
Angellotti A, Marras G, Morana M, Chariton S, Stopponi V, Medeghini L, Romano C, Correale A, Bindi L, Kaminsky FV and Stagno V (2025) Lithospheric origin of a diamond from the Rio Sorriso area, Mato Grosso State, Brazil. *Front. Geochem.* 3:1607472. doi: 10.3389/fgeoc.2025.1607472

Lithospheric origin of a diamond from the Rio Sorriso area, Mato Grosso State, Brazil

A. Angellotti[1], G. Marras[1]*, M. Morana[2], S. Chariton[3], V. Stopponi[4], L. Medeghini[1], C. Romano[5], A. Correale[6], L. Bindi[2], F. V. Kaminsky[7] and V. Stagno[1,6]*

[1]Department of Earth Sciences, Sapienza University of Rome, Roma, Italy, [2]Department of Earth Sciences, University of Florence, Firenze, Italy, [3]Center for Advanced Radiation Sources, The University of Chicago, Chicago, IL, United States, [4]CNR - Istituto Officina dei Materiali (IOM), Trieste, Italy, [5]Department of Science, University of Roma Tre, Rome, Italy, [6]Istituto Nazionale di Geofisica e Vulcanologia, Palermo, Italy, [7]Vernadsky Institute of Geochemistry and Analytical Chemistry, Russian Academy of Science, Moscow, Russia

Diamonds are unique samples that enlarge our vision of the physical and chemical reactions occurring in Earth's deep, inaccessible mantle. By investigating the minerals and fluids trapped within them, it is possible to ascertain the key conditions relevant to diamond formation, such as pressure, temperature, and oxygen fugacity. In this study, we investigated a diamond from the Rio Sorriso area, Juína (Brazil), a site known for the high abundance of sublithospheric diamonds discovered there. The diamond contained both colorless and greenish optically visible inclusions of Na–Cr-bearing diopside, high-Mg olivine, and enstatite. Thermobarometric estimates of the polished and entrapped inclusions suggest that the diamond likely formed at pressures between 4 and 5 GPa and temperatures of 1,050 °C–1,150 °C. Major and trace elements data from one polished clinopyroxene provide evidence of interaction between the local peridotite and an oxidized Na-rich carbonated melt—a generally proposed growth medium from which diamonds may have crystallized. Our study thus demonstrates that diamonds from underneath the Amazonian craton did not originate solely at lower mantle depths but also within a metasomatized lithospheric mantle.

KEYWORDS

thermobarometry, redox, synchrotron Mössbauer, metasomatism, Amazonian craton

1 Introduction

The investigation of mineral inclusions in diamonds, although infrequent, represents a fundamental tool for shedding light on the fluid-mediated processes that affect the deep volatile cycle at the local scale (Stagno and Fei, 2020). In 2008, analysis of 2,844 inclusion-bearing lithospheric diamonds revealed high affinity for peridotite (P-type)-like mineral assemblages (65%), followed by eclogite (E-type)-like inclusions (33%; Stachel and Harris, 2008). P-types exhibiting extensive melting, such as harzburgitic inclusions, have been frequently reported, while those recording refertilization, such as wehrlitic inclusions, are rare, representing only 0.2% of samples. In a recently updated dataset, Stachel et al. (2022) reported a total of 20 wehrlitic inclusions for 12 diamonds extracted from cratonic locations such as Buffalo Head (Banas et al., 2007), Superior (Stachel et al., 2018), Kalahari (Daniels and Gurney, 1999; Viljoen et al., 2014), Kimberley (Jaques et al., 1989), and Yakutia

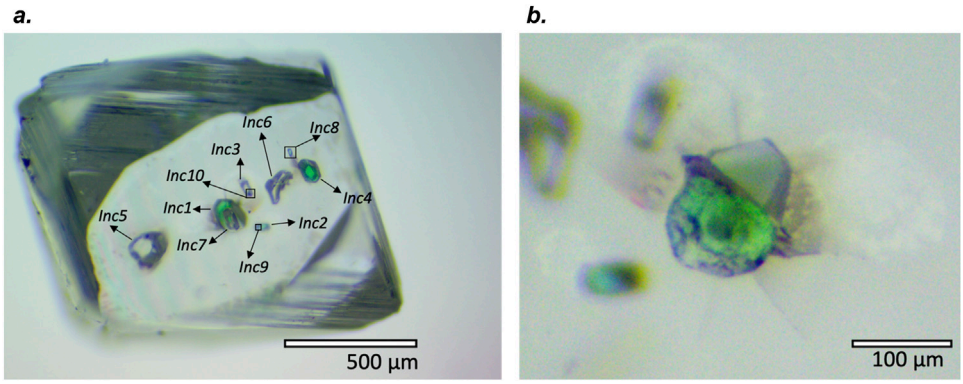

FIGURE 1
(a) Optical image of COMSK3 diamond and the ten visible inclusions. **(b)** Detail of *Inc1* showing the slightly inclined orientation underneath the diamond surface.

(Sobolev et al., 1977; 2004). For these inclusions (Supplementary Table S1), a wehrlitic (deep) origin has been proposed based on the CaO and Cr_2O_3 content of the entrapped garnet (grt) according to the proper classification scheme (Grütter et al., 2004). Additional inclusions are represented by olivine (ol) and clinopyroxene (cpx). Interestingly, some of the listed diamonds could be classified as type IaAB, thereby allowing nitrogen-based thermometric analyses, which resulted in residence temperatures (T) between approximately 1,070 °C and 1,320 °C (Stachel et al., 2022). On the other hand, a wehrlitic component has been proposed in the case of diamonds with a mixed paragenesis (i.e., eclogitic and wehrlitic), such as in the case of type II K14 diamond (Buffalo Head Terrane; Davies et al., 2004), type IaAB diamond Gahcho Kue (Slave Craton; Stachel et al., 2022), and type IaA Childliak (Hall Peninsula; Stachel et al., 2022). No lithospheric diamond inclusions have been reported from the Rio Sorriso area, Juína (Brazil). Diamonds from Rio Sorriso, in the Amazonian Craton, have been classified as sublithospheric, a type known for having originated at lower mantle depths (Hayman et al., 2005; Kaminsky et al., 2023). In contrast, some mantle xenoliths from the same area, transported to the surface by kimberlitic volcanism (92–95 Ma in age; Heaman et al., 1998; Cabral-Neto et al., 2025), present both peridotitic and eclogitic mineralogy. A recent study, based on the exceptional age of sublithospheric Juína diamonds, dates their formation to 610–450 Ma from a peri-Gondwanan subduction system, followed by their upwelling to the lithospheric keel of the Gondwana supercontinent and subsequent continental accretion and break-up (Timmerman et al., 2023).

This study reports analyses of the first lithospheric diamond from Rio Sorriso containing at least ten visible mineral inclusions (Figure 1a), one of which polished to the surface (Figure 1b). We employed several techniques, including *in situ* analyses, to investigate the chemistry (i.e., major and trace elements and the iron oxidation state) and mineralogy of the inclusions in order to determine the pressure, temperature, and redox (P-T-fo_2) conditions of entrapment along with the composition of the growth medium. The combination of several techniques applied to a single diamond enables unique mineral characterization (Sobolev et al., 2000; Pearson et al., 2014; Nestola et al., 2017; Nestola et al., 2019; Tschauner et al., 2021; Carvalho et al., 2024) and a better understanding of the redox processes at the time of diamond formation (Jacob et al., 2016; Chen et al., 2018; Anzolini et al., 2020; Nestola et al., 2023). Our study not only contributes to the actual dataset but also represents the first report of the possible existence of lithospheric diamonds underneath the Amazonian craton, with evidence of metasomatic fluid–rock interactions.

2 Materials and methods

2.1 Macroscopic description and major and trace element analyses of the investigated diamond

The lithospheric diamond (COMSK3) under investigation is octahedral, with two polished parallel surfaces cut along the [100] crystallographic face, measuring approximately 1.3 × 1.6 mm with a thickness of ~0.6 mm. The diamond contains ten visible colorless and pale-green mineral inclusions (hereafter, *Inc*) ranging in size from 0.02 to 0.2 mm (Figures 1a,b). The images of the diamond and its inclusions were acquired using an AmScope stereoscope under reflected and transmitted light, while birefringence colors were observed under polarized light with a Leica DM750 microscope (Supplementary Figure S1a-c). Both microscopes are equipped with their own high-resolution camera, and the images were collected with integrated software provided by the manufacturer.

Textural and morphological analyses on the exposed inclusion (Supplementary Figure S2a) were performed with a ZEISS EVO MA10 scanning electron microscope (SEM) at the CNR- Istituto di Geologia Ambientale e Geoingegneria (IGAG; Sapienza University of Rome, Italy), which is equipped with an AZTEC-integrated energy-dispersive X ray spectrometer (EDS). The analyses were performed with 20 kV and 50 pA, using cobalt as standard. The chemical analyses on *Inc1* (Supplementary Figure S2b; Supplementary Table S2) were performed using a JEOL JXA-8230 electron probe microanalyzer (EPMA) equipped with five spectrometers at the Department of Earth Sciences of the University of Florence (Italy). An accelerating voltage of 15 kV and 20 nA with a defocused electron beam of 3 µm diameter size were used. Oxides and silicates were employed as standards: albite

for Si and Na, olivine for Mg, plagioclase and garnet for Al, bustamite for Mn, diopside for Ca, ilmenite (Smithsonian standard) for Ti and Fe, chromite for Cr, and sanidine for K. Chemical maps were also acquired (Supplementary Figure S3). Trace element analyses of the exposed *Inc1* (Supplementary Table S2) were performed by laser ablation inductively coupled plasma mass spectrometry (LA-ICPMS) with an Agilent-7500 CX plasma mass spectrometer at the Istituto Nazionale di Geofisica e Vulcanologia (INGV) of Palermo (Italy). The analyses were performed with a constant laser frequency rate of 10 Hz, fluency of 15 J/cm^2, and He flux of 0.8 L min^{-1} in the ablation cell. A diameter of 32 μm for the laser spot was used during the ablation. One analysis each was conducted in the core and rim of *Inc1*, while the background was collected from two spots on the surface of the diamond host. The accuracy of the analyses (RSD%) was calculated by repeated analysis of the USGS basaltic reference glass BCR-2G and was ≤ 15% for all the elements.

2.2 *In situ* synchrotron Mössbauer spectroscopy

The Fe oxidation state of three mineral inclusions, one exposed to the polished surface (*Inc1)* and two entrapped (*Inc2* and *Inc5*), was determined by *in situ* synchrotron Mössbauer spectroscopy at the beamline ID18 (Rüffer and Chumakov, 1996) of the European Synchrotron Radiation Facility (ESRF) in Grenoble (France). The typical energy for the Mössbauer effect at 14.4 keV was obtained through the (111) Bragg reflection of a $^{57}FeBO_3$ crystal mounted on a Wissel velocity transducer driven with a sinusoidal wave form (Potapkin et al., 2012). The beam was focused to an area of 6 × 15 μm^2 using Kirkpatrick–Baez mirrors. The velocity scale of ±6 mm/s was calibrated using an α-Fe foil of 25 μm of thickness. The spectra were acquired within 2.5 and 4.5 h and fitted using a pseudo-Voigt line shape with MossA software (Prescher et al., 2012). Nestola et al. (2016) and Marras et al. (2023) described the advantage of this technique, which consisted of a much higher spatial resolution of the measurement (~15 μm) than the Mössbauer milliprobe source that, in turn, allows the acquisition of $Fe^{3+}/\Sigma Fe$ values from multiple inclusions either entrapped or exposed. Supplementary Figures S4a–c show the spectra of *Inc1* and *Inc2*, collected in approximately 4.5 h and 2.5 h, respectively, and of *Inc5*, collected in 2.5 h. The Mössbauer spectra of cpx inclusions were fitted with two doublets for Fe^{2+} and one for Fe^{3+}, following Canil and O'Neill (1996) and Stagno et al. (2015). The component area ratios of the Fe^{2+} doublets were left unfixed but constrained to the same value to account for the preferred crystal orientation (McCammon et al., 2000). The spectrum of ol was also fitted with two doublets for Fe^{2+} and one for Fe^{3+}. The tiny contribution of Fe from the Be window was considered by fitting all the spectra with an extra singlet (central shift of 0.3249 mm/s), the position of which was determined through measurements of the background performed during the analytical session. Supplementary Table S4 summarizes the hyperfine parameters for each of the three analyzed minerals and the calculated $Fe^{3+}/\sum Fe$. The quadrupole splitting (QS) and center shift (CS) are reported in Supplementary Figures S5a and b (cpx and ol, respectively) along with the known hyperfine parameter for ol (Canil and O'Neill, 1996; Ejima et al., 2018; Marras et al., 2023), for peridotitic cpx (Canil and O'Neill, 1996), for natural eclogitic cpx, and for synthetic eclogitic cpx (Stagno et al., 2015) (Supplementary Table S4). Hyperfine parameters for eclogitic cpx inclusions in diamonds (McCammon et al., 1998) are also shown in Supplementary Table S4.

2.3 Raman and μ-FTIR spectroscopy

The Horiba LabRam HR 800 Raman spectrometer at the University of Roma Tre (Rome, Italy) was used to identify the entrapped mineral inclusions, infer their chemical composition, and verify the presence of residual stress. A total of 57 spectra were acquired in the range of 100–4,000 cm^{-1} from eight of the ten inclusions, one of which (*Inc6*) appeared to consist of two smaller inclusions (*Inc6a* and *Inc6b*). The instrument is equipped with an attenuated doubled Nd^{3+}: YAG laser with a wavelength of 532 nm and an optical microscope. The laser power on the sample surface was 60 mW, and the analyses were performed with a 100× objective and 5 μm^2 spot size. Pure silicon was used as a standard. Instrumental settings consisted of 600 grooves/mm grating density, a confocal hole of 300 μm, and a slit of 200 μm, with an exposure time of 60 s. Each collected spectrum was the average of three acquisitions to improve the signal-to-noise ratio. The acquired spectra were preliminarily compared with those available from the RUFF database (Lafuente et al., 2015). The precise positions of the spectral bands were determined through deconvolution using PeakFit software. Supplementary Figures S6a–h show the collected spectra along with the zoomed image of the analyzed inclusions. Spectra for *Inc8* and *Inc9* are not shown due to their low-quality signal caused by the small sizes (less than 20 μm) of the inclusions. To account for the temporal drift in the Raman band position, the collected spectra were corrected with respect to the peak at 1,330.4 cm^{-1} measured on the diamond surface. In each of the collected spectra, a broad band appears at ~1,150 cm^{-1}, which we attribute to a residual solvent (i.e., ethanol) used to clean the diamond prior to the Raman analyses. The occurrence of hydroxyl groups could be investigated only in *Inc1* by reflectance micro-Fourier-transform infrared spectroscopy (μ-FTIR) using an IR Nicolet iS50 spectrometer coupled with the Nicolet Continuum IR microscope, available at the Department of Earth Sciences, Sapienza University of Rome, Italy. The spectra were collected in the range of 4,000-650 cm^{-1} with a spatial resolution of 4 cm^{-1} averaged from 300 scans and a 50 × 50-μm spot size. Additional measurements were conducted by transmission μ-FTIR spectroscopy at the Material Science branch of SISSI beamline of CNR-IOM at Elettra Sincrotrone Trieste (Italy) to characterize the host diamond for possible thermometric applications; a smaller and circular detectable area avoids the inference of small inclusions when collecting transmission-mode spectra. The analyses were carried out between 6,000 and 600 cm^{-1} using a Vertex 70 v interferometer coupled with a Hyperion2000 microscope (Bruker Optics), liquid N_2-cooled HgCdTe (MCT) detector, and a KBr beam splitter. Measurements were conducted using the synchrotron source with a resolution of 2 cm^{-1} and an aperture of 30–60 μm by collecting five to ten acquisitions per area of 128 scans each. The μ-FTIR

spectra were elaborated using OPUS and Spectragryph (Menges, 2020) software programs.

2.4 X-ray diffraction and tomographic analyses

Structural information on the entrapped mineral inclusions was acquired by *in situ* synchrotron single-crystal X-ray diffraction (SCXRD) at the GSECARS 13BM-D beamline of the Argonne National Laboratory (Chicago, USA). Prior to the SCXRD measurements, the diamond was scanned, and its inclusions were localized with the help of X-ray computed microtomography (CMT; Supplementary Figure S7) in conjunction with the SCXRD setup at beamline 13BM-D (Sutton et al., 2022). For the CMT measurements, a monochromatic beam at 30 keV was defocused to provide a large field of view on a scintillator plate. A Mitutoyo 5× objective attached to a 75-mm tube allowed a pixel resolution of 2.08 μm. A total of 900 frames with 0.2° step and 2-s exposure was collected as the diamond rotated. Tomographic reconstruction of the projections was carried out with the help of IDL-based software available at the beamline. The reconstructed images were used to accurately place the inclusion of interest in the center of the X-ray rotation. Subsequently, the same monochromatic beam was focused on a 20 × 20 μm beam, and the diffraction setup was automatically railed in. The X-ray diffraction system was equipped with a Pilatus 1M CdTe detector. The sample–detector distance was set to 227.91 mm and the energy at 30 keV (λ = 0.4133 Å). SCXRD data collection was performed as a series of ω scans with a step of 0.5° and 10 s exposure/step over a ±35° range. Single-crystal X-ray diffraction data were collected on *Inc1*, *Inc4*, *Inc5*, *Inc6a*, and *Inc6b*; the unit-cell parameters are reported in Supplementary Figure S5. The crystallinity of the targeted inclusion was initially verified using Dioptas (Prescher and Prakapenka, 2015), followed by further analysis of the unit-cell determination, integration of the reflection intensities, and empirical absorption correction using the CrysAlisPro software package. The refinements were performed using SHELXL (Sheldrick, 2015). Charged scattering curves (Prince, 2004) were employed in the refinement of the olivine crystal structures. EosFit-Pinc software (Angel et al., 2017) was employed to determine the final pressure of the inclusion at ambient conditions (P_{inc}) and pressure of entrapment (P_{trap}).

3 Results

3.1 Optical, textural, and chemical analyses of the inclusions

The diamond examined under polarized transmitted light revealed a typical birefringence (Lang, 1967; Howell et al., 2012) which consisted of the formation of strain-nodules caused by the stressed *Inc4* and *Inc5* (Supplementary Figure S1a). Supplementary Figures S1b and c show the (sub)euhedral shape of the inclusions varying from rounded (*Inc5*; Supplementary Figure S1b) to prismatic (*Inc6*; Supplementary Figure S1c). These images highlight both the presence of composite inclusions (e.g., *Inc6* is composed of two tiny inclusions, *Inc6a* and *Inc6b*, positioned ~120° from each other) and the occurrence of tiny radial fractures departing from the inclusions, which are generally much shorter than the inclusion size, along with a dark brownish and wavy rim. Some inclusions are rimmed by dark halos, interpreted by Agrosì et al. (2019) as the residue of carbonate-bearing fluids from which the diamond might have formed. Striations, commonly referred to as stepped-face growth, are visible on the external surface of the diamond (Supplementary Figure S8) and represent resorption features formed during transport by oxidized ascending magma (Fedortchouk et al., 2019). The textural analysis of the exposed polished inclusion *Inc1* shows the presence of radial fractures and a (sub)euhedral shape (Figure 1b). The chemical analysis of the polished inclusion (Supplementary Table S2) appears homogeneous, which is also confirmed by compositional maps (Supplementary Figure S3). The core-to-rim chemical composition of *Inc1* shows a slight decrease of MgO (from 14.00 to 13.47 wt%), CaO (from 14.30 to 13.98 wt%), and Na_2O (from 3.79 to 3.68 wt%), while the other oxides remain constant within the uncertainty of the measurement. The obtained average composition calculated from the four analyses, with totals close to 100 wt%, is 54.82 (±0.63) wt% SiO_2, 0.04 (±0.01) wt% TiO_2, 2.57 (±0.05) wt% Al_2O_3, 6.33 (±0.08) wt% Cr_2O_3, 1.82 (±0.06) wt% FeO, 0.05 (±0.01) wt% MnO, 13.61 (±0.32) wt% MgO, 14.11 (±0.23) wt% CaO, 3.73 (±0.07) wt% Na_2O, and 0.50 (±0.01) wt% K_2O. On the basis of six oxygen atoms, the chemical formula of the polished inclusion can be written as

$$(Ca_{0.56}Na_{0.27}K_{0.02}Fe^{2+}_{0.05}Mg_{0.10})(Mg_{0.69}Cr^{3+}_{0.19}Al_{0.11}Fe^{3+}_{0.01})Si_{2.00}O_6,$$

identified as a diopside with ~20% of kosmochlor ($NaCrSi_2O_6$) component and ratios of Cr/(Cr + Al) (Cr) of 0.63 and Mg/(Mg + Fe) (Mg#) of 0.93.

3.2 Spectroscopic identification of the inclusions and diamond classification

Inc1, *Inc2*, and *Inc4* (Supplementary Figures S6a,b,d) exhibit the characteristic vibrational features of a diopside with major peaks at 333–341, 403–407, and 558–564 cm^{-1} related to metal-oxygen translation, 672–678 cm^{-1} (ν11) caused by stretching vibrations of bridging O–Si–O atoms, and 1,014–1,021 cm^{-1} (ν16) caused by stretching vibrations of non-bridging O–Si–O atoms (Chopelas, 1999; Huang et al., 2000; Wang and Gasparik, 2001). The consistency of the vibrational modes, especially for ν11, between *Inc1, Inc2, and Inc4* (Supplementary Table S6) might indicate that they all have the same chemical composition. According to the parametrization of the Raman shift of ν11 as a function of CaO, MgO, Na_2O, Al_2O_3, and Cr# (Kalugina and Zedgenizov, 2020), these Cr-clinopyroxene inclusions have compositions between peridotitic and eclogitic, with low Al_2O_3 content of approximately 3 wt% calculated as

$$Al_2O_3\ (wt\%) = 0.81\ (\pm\ 0.05) \cdot \nu11 - 545.2\ (\pm\ 37.2). \quad (1)$$

The spectra collected from *Inc5*, *Inc6a*, and *Inc6b* (Supplementary Figures S6e–f) are consistent with olivine (Chopelas, 1991). The position of bands at 826 cm^{-1} and 857 cm^{-1} correlate with the Mg# (but also with P). According to

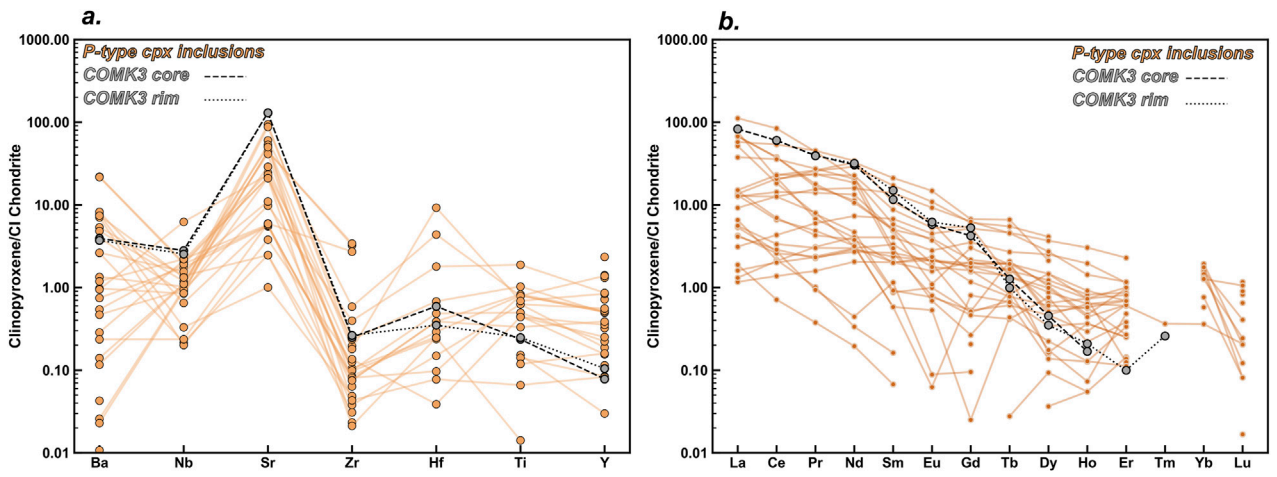

FIGURE 2
(a) Concentration of selected trace elements in the *Inc1* cpx from the core (dashed line) and rim (dotted line) normalized to the CI chondrite (McDonough and Sun, 1995) and compared with concentrations of P-type (orange) cpx inclusions available in the dataset (Stachel et al., 2022). **(b)** REE concentrations in *Inc1* cpx (core, dashed line and rim, dotted line) normalized to the CI chondrite and compared with P-type (orange).

the available parameterizations (Kuebler et al., 2006; Yasuzuka et al., 2009), these three inclusions have Mg# > 90, which is further supported by the appearance of a band at ~610 cm^{-1}, typical of forsteritic olivine. The Raman spectra of *Inc3*, *Inc7*, and *Inc10* (Supplementary Figures S6c, g, h; Supplementary Table S6) are representative of (ortho)enstatite with Mg# of 90 (Huang et al., 2000). The presence of additional bands at 368 cm^{-1} (*Inc3*) and 367 cm^{-1} (*Inc10*), identifiable only by peak deconvolution, can however be interpreted as characteristic of clinoenstatite (Cen; Ulmer and Stader, 2001). In conclusion, few variations of the main bands in some inclusions are observed with respect to those from the literature; these can be explained as the effect of either the chemical composition or some possible residual stress of those inclusions entrapped in the diamond. The infrared (IR) spectrum (Supplementary Figure S9a) shows no defect-induced absorption in the 1,500-500 cm^{-1} region, which excludes the presence of N and H in the diamond with the two-phonon absorption characteristic of type II diamonds in the 2,800-1,500 cm^{-1} spectrum. No evidence of molecular H_2O was found in *Inc1* (Supplementary Figure S9b).

3.3 Trace element composition of polished *Inc1*

The concentration of trace elements in *Inc1* (Supplementary Table S3) between core and rim is within uncertainty, such as Sr with 939 ppm (942 ppm at the rim), Ti with 104 ppm (109 ppm at the rim), Mn with 663 ppm, V with 543 ppm (539 ppm at the rim), Ni with 338 ppm (331 ppm at the rim), Ce with 37 ppm, and Sc with 31 ppm. Hence, no significant variations occur between the rim and core of *Inc1*. Figure 2a shows the abundance of seven analyzed trace elements at the core and rim of *Inc1*, normalized to the carbonaceous Ivuna chondrite used as reference (Stachel et al., 2022; McDonough and Sun, 1995) and plotted along with those from 30 lherzolitic inclusions with the aim of reconstructing the possible petrological history of the inclusions and, hence, of the diamond. The trace element distribution is consistent with published data for lherzolitic P-type inclusions (Stachel et al., 2022). The (CI chondrite-) normalized rare earth elements (REE) are shown in Figure 2b, where the typical steep trend for light rare earth elements (LREE) agrees with that reported for lherzolitic cpx inclusions and would indicate coexistence with garnet in the diamond-forming mineral assemblage (Stachel et al., 2022).

3.4 Iron oxidation state of trapped clinopyroxene and olivine inclusions

Very few $Fe^{3+}/\sum Fe$ data exist for the tiny minerals entrapped in diamonds that might shed light the redox environment where diamonds grew. Here, *in situ* synchrotron Mössbauer analyses were performed to determine the $Fe^{3+}/\sum Fe$ ratio of two cpx crystals (*Inc1* polished to the surface, *Inc2* entrapped) and one entrapped ol (*Inc5*). The calculated $Fe^{3+}/\sum Fe$ ratio in *Inc1* is 0.16 (±0.03), 0.14 (±0.02) in *Inc2*, but 0.02 (±0.01) in *Inc5* (Supplementary Figure S4). These data agree with the only available data for $Fe^{3+}/\sum Fe$, varying from 0.08 to 0.14, in cpx diamond inclusions from George Creek (McCammon et al., 1998). When compared with $Fe^{3+}/\sum Fe$ ratio of cpx from mantle rocks (Supplementary Table S7), we notice that spinel (spl)-peridotites (95 samples; Luth and Canil, 1993) have cpx with $Fe^{3+}/\sum Fe$ that ranges between 0.03 and 0.35 (0.24–0.29 is the most frequent interval); cpx crystals in grt-peridotites (22 samples; Luth and Canil, 1993; Woodland et al., 2006) have $Fe^{3+}/\sum Fe$ between 0.09 and 0.44 (0.24–0.29 is the most frequent interval), while cpx crystals from eclogites (63 samples Mikhailenko et al., 2020) have $Fe^{3+}/\sum Fe$ varying between 0.05 and 0.63 (0.15–0.24 being the most frequent interval). Finally, $Fe^{3+}/\sum Fe$ of wehrlitic cpx crystals (3 samples) vary from 0.16 to 0.21. Our measured $Fe^{3+}/\sum Fe$ in cpx is also compared with that of synthetic cpx equilibrated at high P, T, and fo_2 of dry eclogitic

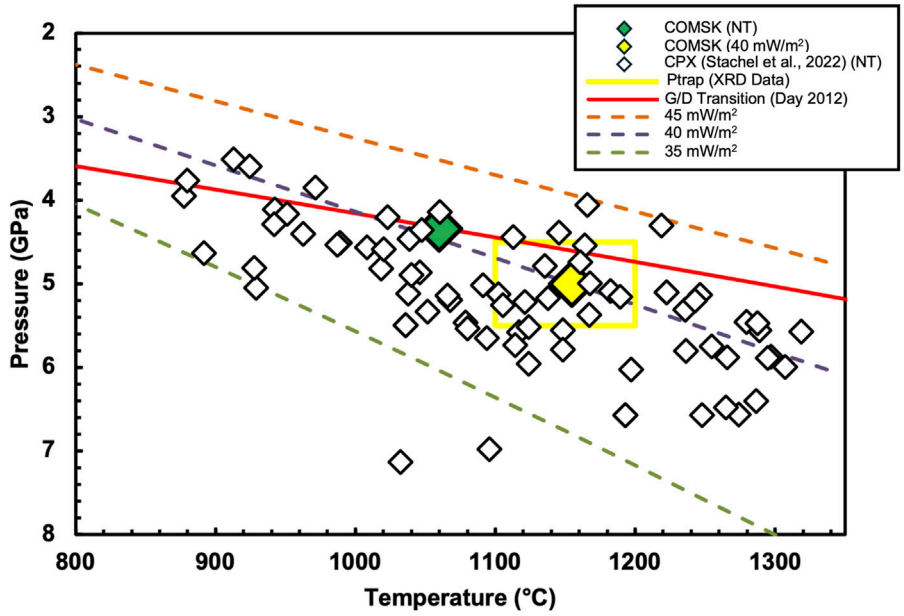

FIGURE 3
P-T conditions determined for inclusions of cpx from Stachel et al. (2022) and for the COMSK3 diamond using the cpx-thermobarometer (see text) plotted along with three geotherms taken as reference including the 40 mW/m² for the Amazonian craton (Chagas de Melo et al., 2025). The graphite–diamond boundary is also shown.

assemblages. The $Fe^{3+}/\sum Fe$ of eclogitic cpx varies between 0.13 and 0.24 under the carbon–carbon dioxide (CCO) buffer (Purwin et al., 2013) and 0.04 to 0.19 under the carbon–carbonate buffer (Stagno et al., 2015), respectively. It is, therefore, difficult to infer a possible interaction between cpx and oxidized fluid just by looking at the $Fe^{3+}/\sum Fe$. The $Fe^{3+}/\sum Fe$ measured on the ol of *Inc5* is consistent with the literature (Ejima et al., 2018; Marras et al., 2023).

3.5 Thermobarometric determinations

Elastic geobarometry allows the calculation of the conditions of entrapment, exploiting the difference in elastic properties between the host and the inclusion starting from the residual pressure on the latter—*Pinc* (Angel et al., 2022). Olivine inclusions in diamonds have been employed as geobarometers to infer the growth conditions of the diamond host (Nestola et al., 2011). The unit-cell volume that the ol inclusion would have at room pressure V_0 is needed to determine P_{inc}, and it depends on the Mg# (0.93 for *Inc5* and *Inc6b*, and 0.92 for *Inc6a*, all obtained here by *in situ* structure refinement and Raman spectroscopy). For *Inc6a*, isotropic approximation was employed due to the lower number of available reflections (Supplementary Table S8). We calculated V_0 using two different equations: a linear regression (Wang et al., 2023) and the equation proposed by Schwab and Küstner (1977). The resulting P_{inc} of 0.4–1.1 GPa was calculated using the third-order Birch–Murnaghan equation of states (EoS) isothermal model for olivine (Angel et al., 2018), taken as minimum and maximum values by combining the two models in Supplementary Table S9. From P_{inc}, a pressure of entrapment, P_{trap}, was calculated using the EoS for diamond (Angel et al., 2015). From the three ol inclusions, applying a temperature of entrapment, T_{trap}, of both 1,100 °C and 1,200 °C results in *Ptrap* of 5.2 and 5.5 GPa, respectively, using the linear regression, and 4.5 and 4.7 GPa, respectively (Schwab and Küstner, 1977). The available dataset of inclusions in diamond (Stachel et al., 2022) reports 14 diamond samples with only cpx crystals found as inclusion. Among these diamonds, one is type II and four have no analyses of N aggregation. Temperature estimates vary from 1,116 °C to approximately 1,370 °C using the available geothermobarometer of Nimis and Taylor (2000) and Nimis et al. (2020). In this study, thermobarometry on *Inc1* gives T of 1,060 °C and P of 4.3 GPa, the latter being consistent with a P range of 4.5 and 5.5 GPa obtained by elastic barometry on *Inc5*, *Inc6a*, and *Inc6b*. By projecting the mid-pressure value of 5 GPa on the 40 mW/m² geotherm of the Amazonian craton, we obtained an independent T of 1,155 °C, which is consistent with a T range of 1,170 °C–1,300 °C proposed for the Juína area aged approximately 2 Ga (Bulanova et al., 2010). These thermobarometric estimates are reported in Figure 3 along with the P-T conditions equally determined for those diamonds where only cpx inclusions have been reported. The P-T conditions for COMSK3 fall below the graphite–diamond transition line (Day, 2012).

4 Discussion

4.1 Na-rich, CO_2-rich melt as a diamond-forming medium?

Typical diagrams have been used to distinguish peridotitic from eclogitic cpx inclusions in lithospheric diamonds on the basis of their major elements, such as Cr, Ti, Ca, Na, Al, Mg, Fe, and Cr (Figures 4a–c). The deviation from the proposed P- and E-type fields as well as differences with respect to the composition of cpx from

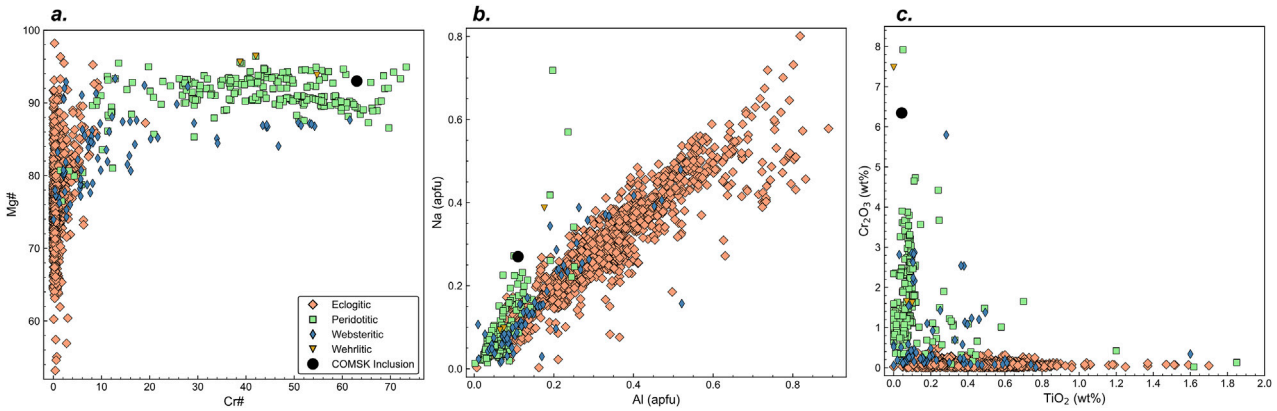

FIGURE 4
(a) Mg# plotted against Cr#, **(b)** Na (apfu) against Al (apfu), and **(c)** Cr_2O_3 (wt%) against TiO_2 (wt%) of *Inc1* cpx (black circle) compared with the composition of cpx diamond inclusions available in the literature.

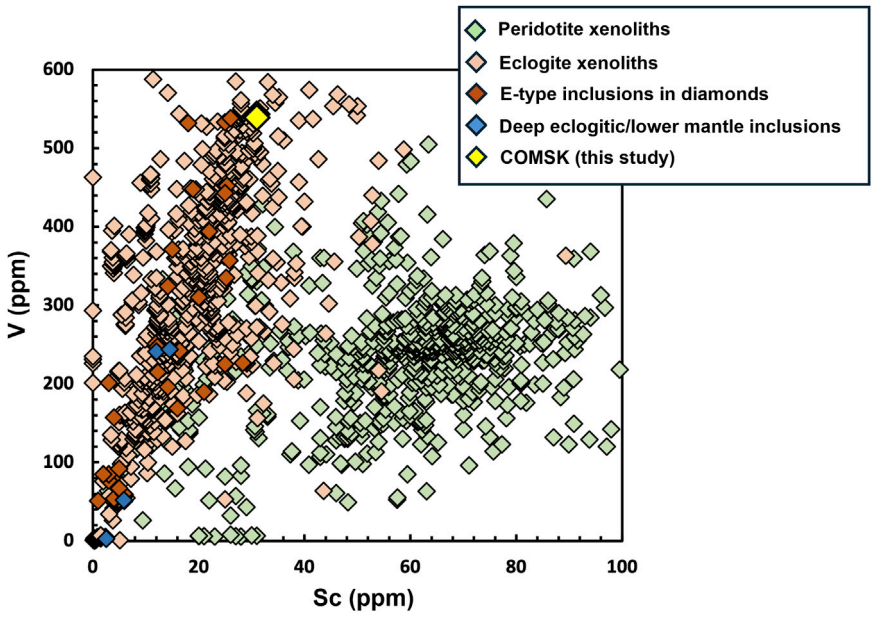

FIGURE 5
Concentration of V (ppm) plotted against Sc (ppm) in COMSK3 cpx and in cpx inclusions in diamonds along with in peridotitic and eclogitic cpx in mantle xenoliths (GEOROC Database updated at 03/01/2024).

mantle peridotites are evidence of metasomatic reactions (Mikhail et al., 2021; Stachel et al., 2022). The concentration of trace elements in diamond inclusions (LREE/HREE, Ce/Nb, Nd/Dy, Zr/Hf, and Ti/Eu) is also indicative of metasomatism, with a strong dependence on the chemical composition of the reactive fluid (Stachel and Harris, 1997; Stachel et al., 2022). The major elements for the exposed *Inc1* were compared with the available chemical dataset for cpx inclusions in lithospheric diamonds. While the Mg# and Cr# of *Inc1* cpx falls within the characteristic range of the peridotitic suite (Figure 4a), the Na and Al contents (expressed in atoms per formula units, apfu) lie in between peridotitic and eclogitic compositions (Figure 4b; Equation 1). The average values of Cr_2O_3 (6.3 wt%) along with the high CaO content (14.11 wt%) of *Inc1* are typical concentrations of some wehrlitic garnets (Sobolev et al., 1973). These values deviate from the typical values found in cpx inclusions in peridotitic and eclogitic suite (Figure 4c), with the exception of few cpx, such as D1364A (Daniels and Gurney, 1999) and Kmsm-6 and Kmsm-7 from Yakutian wehrlitic diamonds (Sobolev et al., 1977; 2004). Both the major (e.g., Na, Cr, and Al) and trace (e.g., V and Sc) element composition of the entrapped cpx suggest a refertilization process similar to that recorded by cpx formed by (re-)fertilization of spl-bearing peridotite (Aulbach et al., 2020). Wehrlitization processes thus occur through the interaction of a mantle grt harzburgite with a metasomatic CO_2-bearing melt at

1.5–2 GPa, leading to the formation of opx poor/free, cpx-rich rocks through the equilibrium reaction (Wallace and Green, 1988; Yaxley et al., 1998):

$$enstatite + dolomite\ (melt) = diopside + olivine + CO_2\ (vapor) \quad (2)$$

An analog reaction occurring more in-depth is

$$enstatite + dolomite\ (melt) = diopside + olivine + diamond + O_2 \quad (3)$$

that is, equivalent to the fo_2 buffering equilibrium (the acronym is *EDDOD*; Stagno and Frost, 2010) and describes the coexistence of carbonate (either liquid or solid) with diamond in the upper mantle. At the P and T determined from *Inc1*, this equilibrium reaction locally buffers the $\Delta\log fo_2$ at values between −1.3 and −1.6, assuming a reacting (metasomatic) melt varying from Na-bearing dolomitic to carbonate–silicate in composition. The lack of a chemical zonation between rim and core in *Inc1* would support the cpx origin by direct transformation of a preexisting opx rather than by metasomatic contamination of a lherzolitic cpx. Indeed, a recent experimental study (Wang et al., 2022) helps distinguish peridotitic cpx from cpx formed by wehrlitization (Equation 2) on the basis of the variation of the major element composition, which is affected by the nature of the interacting melt, whether carbonatitic or silicic. In the case of *Inc1*, the simultaneous increase of the Ca/Al ratio with Mg# opposite the decreasing trend of Al_2O_3 and TiO_2 are proposed evidence of the formation by interaction with coexisting carbonatitic melts (Equation 3). The high kosmochlor component has been classically considered a marker of *groups 6* and *7* cpx used as mineral indicators for diamond exploration (Quirt, 2004) and related to lithospheric refertilization by Na-rich carbonatite metasomatism of either Cr-rich, grt-bearing peridotites (Grütter et al., 2024) or Cr-rich, spl-bearing peridotites (Ikehata and Arai, 2004). Notably, the V content is much greater than that reported in P-type inclusions (542 ppm; Figure 5). Such enrichment would require crystallization from (or equilibration with) a parental melt with 100–300 ppm of V (Wang et al., 2019) that, in the absence of data for carbonatites, is consistent with 100–300 ppm measured in natural kimberlitic rocks (Kostrovitsky et al., 2023). Thus, the minerals found entrapped in COMSK3 diamonds are representative of a lherzolitic environment, then P-type; however, the enrichment in kosmochlor is possible evidence of fluid–rock interaction as described by reaction (3). The proposed presence of carbonate halos, by analogy with the literature, might be further evidence of CO_2-rich fluids from which diamonds might have formed.

5 Conclusion

- The investigated COMSK3 is a type II lithospheric diamond with P-type lherzolitic inclusions that record (redox) interaction with a Na-rich carbonatitic (or carbonate-silicate) melt within a young lithospheric mantle accreted beneath the Amazonian craton.
- Major and trace elements from protogenetic *Inc1* support the interaction between Na-rich, CO_2-rich melts.
- The $Fe^{3+}/\sum Fe$ ratio in cpx ranges between 0.13 and 0.16, which is higher than expected for cpx that did not undergo oxidation.
- A single diamond might not provide all the answers about lithospheric diamond formation at Juína, but the unique characteristics of this diamond provide insights into such a process when compared with the characteristics of the local lithosphere, which is given by available studies of mantle xenoliths and xenocrysts.

Data availability statement

The original contributions presented in the study are included in the article/Supplementary Material; further inquiries can be directed to the corresponding author.

Author contributions

AA: Formal Analysis, Writing – original draft, Visualization, Methodology, Data curation, Investigation. GM: Investigation, Data curation, Validation, Formal Analysis, Visualization, Writing – original draft, Funding acquisition, Methodology. MM: Methodology, Formal Analysis, Writing – original draft, Investigation. SC: Writing – original draft, Formal Analysis, Visualization, Investigation, Software. VSo: Data curation, Formal Analysis, Software, Writing – original draft. LM: Formal Analysis, Data curation, Writing – original draft. CR: Formal Analysis, Data curation, Writing – original draft. AC: Writing – original draft, Formal Analysis, Data curation. LB: Writing – original draft, Data curation, Validation, Formal Analysis. FK: Data curation, Resources, Writing – original draft, Conceptualization. VSa: Writing – original draft, Project administration, Visualization, Supervision, Validation, Funding acquisition, Conceptualization, Data curation.

Funding

The author(s) declare that financial support was received for the research and/or publication of this article. This work was funded by the Dr. Eduard Gübelin Association for Research and Identification of Precious Stones through the “Dr. Eduard Gübelin Research Scholarship” (GM) and by PRIN MUR HERMES project no. 2022R35X8Z (VS).

Acknowledgments

We thank Eleonora Braschi and Andrea Orlando for their help with EPMA analyses and Matteo Paciucci for his technical assistance with the SEM. We thank Alessandro Frontoni for his technical support during the Raman measurements. We are grateful to Sonja Aulbach for sharing the dataset on the trace elements of diamond inclusions. We are thankful to the beamline staff of ex ID18 of ESRF (Grenoble, France; beamtime ES-1489) for assistance during the experimental session. Part of this work was also performed at SISSI beamline (Elettra Sincrotrone Trieste, Italy) and at GeoSoilEnviroCARS (The University of Chicago, Sector 13), Advanced Photon Source (APS), Argonne National Laboratory. GeoSoilEnviroCARS was supported by the National Science Foundation–Earth Sciences (EAR – 1634415).

Conflict of interest

The authors declare that the research was conducted in the absence of any commercial or financial relationships that could be construed as a potential conflict of interest.

The author(s) declared that they were an editorial board member of Frontiers, at the time of submission. This had no impact on the peer review process and the final decision.

Generative AI statement

The author(s) declare that no Generative AI was used in the creation of this manuscript.

Publisher's note

Supplementary material

The Supplementary Material for this article can be found online at: https://www.frontiersin.org/articles/10.3389/fgeoc.2025.1607472/full#supplementary-material

References

Agrosì, G., Tempesta, G., Mele, D., Caggiani, M. C., Mangone, A., Della Ventura, G., et al. (2019). Multiphase inclusions associated with residual carbonate in a transition zone diamond from juína (brazil). *Lithos* 350, 105279. doi:10.1016/j.lithos.2019.105279

Angel, R. J., Alvaro, M., Nestola, F., and Mazzucchelli, M. L. (2015). Diamond thermoelastic properties and implications for determining the pressure of formation of diamond–inclusion systems. *Russ. Geol. Geophys.* 56, 211–220. doi:10.1016/j.rgg.2015.01.014

Angel, R. J., Mazzucchelli, M. L., Alvaro, M., and Nestola, F. (2017). EosFit-Pinc: a simple GUI for host-inclusion elastic thermobarometry. *Am. Mineralogist* 102, 1957–1960. doi:10.2138/am-2017-6190

Angel, R. J., Alvaro, M., and Nestola, F. (2018). 40 years of mineral elasticity: a critical review and a new parameterisation of equations of state for mantle olivines and diamond inclusions. *Phys. Chem. Minerals* 45, 95–113. doi:10.1007/s00269-017-0900-7

Angel, R. J., Alvaro, M., and Nestola, F. (2022). Crystallographic methods for non-destructive characterization of mineral inclusions in diamonds. *Rev. Mineralogy Geochem.* 88 (1), 257–305. doi:10.2138/rmg.2022.88.05

Anzolini, C., Marquardt, K., Stagno, V., Bindi, L., Frost, D. J., Pearson, D. G., et al. (2020). Evidence for complex iron oxides in the deep mantle from feNi(Cu) inclusions in superdeep diamond. *Proc. Natl. Acad. Sci. U.S.A.* 117 (35), 21088–21094. doi:10.1073/pnas.2004269117

Aulbach, S., Lin, A., Weiss, Y., and Yaxley, G. (2020). Wehrlites from Continental mantle monitor the passage and degassing of carbonated melts. *Geochem. Perspect. Lett.* 15, 30–34. doi:10.7185/geochemlet.2031

Banas, A., Stachel, T., Muehlenbachs, K., and McCandless, T. E. (2007). Diamonds from the buffalo head hills, Alberta: formation in a non-conventional setting. *Lithos* 93 (1-2), 199–213. doi:10.1016/j.lithos.2006.07.001

Bulanova, G. P., Walter, M. J., Smith, C. B., Kohn, S. C., Armstrong, L. S., Blundy, J., et al. (2010). Mineral inclusions in sublithospheric diamonds from collier 4 kimberlite pipe, juina, Brazil: subducted protoliths, carbonated melts and primary kimberlite magmatism. *Contrib. Mineral. Petrol.* 160, 489–510. doi:10.1007/s00410-010-0490-6

Cabral-Neto, I., Pearson, D. G., Ruberti, E., Luo, Y., Stern, R. A., Azzone, R. G., et al. (2025). Age and mantle source characteristics of kimberlite-derived zircons from Brazil revealed by U–pb, Hf and O isotopes. *Min. Petrol.* doi:10.1007/s00710-025-00917-1

Canil, D., and O'Neill, H. (1996). Distribution of ferric iron in some upper-mantle assemblages. *J. Petrol.* 37, 609–635. doi:10.1093/petrology/37.3.609

Carvalho, L. D. V., Stachel, T., Luth, R. W., Locock, A. J., Pearson, D. G., Steele-MacInnis, M., et al. (2024). Dense hydrated Mg-silicates in diamond: implications for transport of H_2O into the mantle. *Sci. Adv.* 10, eadl4306. doi:10.1126/sciadv.adl4306

Chagas de Melo, B., Lebedev, S., Celli, N. L., Gibson, S., de Laat, J. I., and Assumpção, M. (2025). The lithosphere of South America from seismic tomography: structure, evolution, and control on tectonics and magmatism. *Gondwana Res.* 138, 139–167. doi:10.1016/j.gr.2024.10.012

Chen, M., Shu, J., Xie, X., Tan, D., and Mao, H. (2018). Natural diamond formation by self-redox of Ferromagnesian carbonate. *Proc. Natl. Acad. Sci. U.S.A.* 115 (11), 2676–2680. doi:10.1073/pnas.1720619115

Chopelas, A. (1991). Thermal properties of β-Mg2SiO4 at mantle pressures derived from vibrational spectroscopy: implications for the mantle at 400 km depth. *J. Geophys. Res. Solid Earth* 96 (B7), 11817–11829. doi:10.1029/91JB00898

Chopelas, A. (1999). Estimates of mantle relevant clapeyron slopes in the MgSiO3 system from high-pressure spectroscopic data. *Am. Mineralogist* 84 (3), 233–244. doi:10.2138/am-1999-0304

Daniels, L. R. M., and Gurney, J. (1999). "Diamond inclusions from the dokolwayo kimberlite,", 1. Swaziland: Extended Abstracts.

Davies, R. M., Griffin, W. L., O'Reilly, S. Y., and McCandless, T. E. (2004). Inclusions in diamonds from the K14 and K10 kimberlites, buffalo hills, Alberta, Canada: diamond growth in a plume? *Lithos* 77 (1-4), 99–111. doi:10.1016/j.lithos.2004.04.008

Day, H. W. (2012). A revised diamond-graphite transition curve. *Am. Mineralogist* 97, 52–62. doi:10.2138/am.2011.3763

Ejima, T., Osanai, Y., Akasaka, M., Adachi, T., Nakano, N., Kon, Y., et al. (2018). Oxidation states of Fe in constituent minerals of a spinel lherzolite xenolith from the tariat depression, Mongolia: the significance of Fe3+ in olivine. *Minerals* 8 (5), 204. doi:10.3390/min8050204

Fedortchouk, Y., Liebske, C., and McCammon, C. (2019). Diamond destruction and growth during mantle metasomatism: an experimental study of diamond resorption features. *Earth Planet. Sci. Lett.* 506, 493–506. doi:10.1016/j.epsl.2018.11.025

Grütter, H. S., Gurney, J. J., Menzies, A. H., and Winter, F. (2004). An updated classification scheme for mantle-derived garnet, for use by diamond explorers. *Lithos* 77 (1-4), 841–857. doi:10.1016/j.lithos.2004.04.012

Grütter, H., Stachel, T., Sarkar, C., and Pearson, G. (2024). "Sodic Cr-diopside compositions record profound pyroxenite/megacrystic (re)fertilization of the central superior craton lithosphere, attawapiskat kimberlites,", 12. Ontario, Canada: Extended Abstracts.

Hayman, P. C., Kopylova, M. G., and Kaminsky, F. V. (2005). Lower mantle diamonds from rio soriso (juina area, Mato Grosso, Brazil). *Contrib. Mineral. Petrol.* 149, 430–445. doi:10.1007/s00410-005-0657-8

Heaman, L., Teixeira, N. A., Gobbo, L., and Gaspar, J. C. (1998). "U-Pb mantle zircon ages for Kimberlites from the juína and paranatinga provinces,", 7. International Kimberlite Conference Extended Abstracts, 322–324. doi:10.29173/ikc2723

Howell, D., Wood, I. G., Nestola, F., Nimis, P., and Nasdala, L. (2012). Inclusions under remnant pressure in diamond: a multi-technique approach. *Eur. J. Mineralogy* 24, 563–573. doi:10.1127/0935-1221/2012/0024-2183

Huang, E., Chen, C. H., Huang, T., Lin, E. H., and Xu, J. A. (2000). Raman spectroscopic characteristics of mg-fe-ca pyroxenes. *Am. Mineralogist* 85, 473–479. doi:10.2138/am-2000-0408

Ikehata, K., and Arai, S. (2004). Metasomatic formation of kosmochlor-bearing diopside in peridotite xenoliths from north island, New Zealand. *Am. Mineralogist* 89 (10), 1396–1404. doi:10.2138/am-2004-1006

Jacob, D., Piazolo, S., Schreiber, A., and Trimby, P. (2016). Redox-freezing and nucleation of diamond *via* magnetite formation in the Earth's mantle. *Nat. Commun.* 7, 11891. doi:10.1038/ncomms11891

Jaques, A. L., Sheraton, J. W., Hall, A. E., Smith, C. B., Sun, S. S., Drew, R., et al. (1989). "Composition of crystalline inclusions and C-isotopic composition of argyle and ellendale diamonds,", 4. International Kimberlite Conference Extended Abstracts, 426–428. doi:10.29173/ikc1192

Kalugina, A. D., and Zedgenizov, D. A. (2020). Micro-raman spectroscopy assessment of chemical compounds of mantle clinopyroxenes. *Minerals* 10 (12), 1084. doi:10.3390/min10121084

Kaminsky, F. V., Zedgenizov, D. A., Sevastyanov, V. S., and Kuznetsova, O. V. (2023). Distinct groups of Low- and High-Fe ferropericlase inclusions in super-deep diamonds: an example from the juina area, Brazil. *Minerals* 13 (9), 1217. doi:10.3390/min13091217

Kostrovitsky, S., Dymshits, A., Yakovlev, D., Sun, J., Kalashnikova, T., Ashchepkov, I., et al. (2023). Primary composition of kimberlite melt. *Minerals* 13 (11), 1404. doi:10.3390/min13111404

Kuebler, K. E., Jolliff, B. L., Wang, A., and Haskin, L. A. (2006). Extracting olivine (Fo–Fa) compositions from raman spectral peak positions. *Geochimica Cosmochimica Acta* 70 (24), 6201–6222. doi:10.1016/j.gca.2006.07.035

Lafuente, B., Downs, R. T., Yang, H., and Stone, N. (2015). "The power of databases: the RRUFF project," in *Highlights in mineralogical crystallography*. Editors T. Armbruster, and R. M. Danisi (Berlin, Germany: W. De Gruyter), 1–30. doi:10.1515/9783110417104-003

Lang, A. R. (1967). Causes of birefringence in diamond. *Nature* 213, 248–251. doi:10.1038/213248a0

Luth, R. W., and Canil, D. (1993). Ferric iron in mantle-derived pyroxenes and a new oxybarometer for the mantle. *Contributions Mineralogy Petrology* 113, 236–248. doi:10.1007/BF00283231

Marras, G., Carnevale, G., Caracausi, A., Rotolo, S. G., and Stagno, V. (2023). First measurements of the Fe oxidation state of spinel inclusions in olivine single crystals from vulture (italy) with the *in situ* synchrotron micro-Mössbauer technique. *Eur. J. Mineral.* 35 (4), 665–678. doi:10.5194/ejm-35-665-2023

McCammon, C. A., Chinn, I. L., Gurney, J. J., and McCallum, M. E. (1998). Ferric iron content of mineral inclusions in diamonds from george creek, Colorado determined using mössbauer spectroscopy. *Contrib. Mineral. Petrol.* 133, 30–37. doi:10.1007/s004100050434

McCammon, C. A., Tennant, W. C., and Miletich, R. (2000). A new method for single crystal measurements: application to mössbauer spectra of mineral inclusions in diamond. *Hyperfine Interact.* 126 (1-4), 241–245. doi:10.1023/A:1012650124159

McDonough, W. F., and Sun, S. S. (1995). The composition of the Earth. *Chem. Geol.* 120, 223–253. doi:10.1016/0009-2541(94)00140-4

Menges, F. (2020). Spectragryph - optical spectroscopy software. Available online at: http://www.effemm2.de/spectragryph/.

Mikhail, S., Rinaldi, M., Mare, E. R., and Sverjensky, D. A. (2021). A genetic metasomatic link between eclogitic and peridotitic diamond inclusions. *Geochem. Persp. Let.* 17, 33–38. doi:10.7185/geochemlet.2111

Mikhailenko, D. S., Stagno, V., Korsakov, A. V., Andreozzi, G. B., Marras, G., Cerantola, V., et al. (2020). Redox state determination of eclogite xenoliths from udachnaya kimberlite pipe (Siberian craton), with some implications for the graphite/diamond formation. *Contrib. Mineral. Petrol.* 175, 107–117. doi:10.1007/s00410-020-01748-3

Nestola, F., Nimis, P., Ziberna, L., Longo, M., Marzoli, A., Harris, J. W., et al. (2011). First crystal-structure determination of olivine in diamond: composition and implications for provenance in the earth's mantle. *Earth Planet. Sci. Lett.* 305, 249–255. doi:10.1016/j.epsl.2011.03.007

Nestola, F., Cerantola, V., Milani, S., Anzolini, C., McCammon, C., Novella, D., et al. (2016). Synchrotron mössbauer source technique for *in situ* measurement of iron-bearing inclusions in natural diamonds. *Lithos* 265, 328–333. doi:10.1016/j.lithos.2016.06.016

Nestola, F., Jung, H., and Taylor, L. (2017). Mineral inclusions in diamonds May be synchronous but not syngenetic. *Nat. Commun.* 8, 14168. doi:10.1038/ncomms14168

Nestola, F., Zaffiro, G., Mazzucchelli, M. L., Nimis, P., Andreozzi, G. B., Periotto, B., et al. (2019). Diamond-inclusion system recording old deep lithosphere conditions at udachnaya (siberia). *Sci. Rep.* 9, 12586. doi:10.1038/s41598-019-48778-x

Nestola, F., Regier, M. E., Luth, R. W., Pearson, D. G., Stachel, T., McCammon, C., et al. (2023). Extreme redox variations in a superdeep diamond from a subducted slab. *Nature* 613, 85–89. doi:10.1038/s41586-022-05392-8

Nimis, P., and Taylor, W. R. (2000). Single clinopyroxene thermobarometry for garnet peridotites. Part I. Calibration and testing of a cr-in-cpx barometer and an enstatite-in-cpx thermometer. *Contrib. Mineral. Petrol.* 139, 541–554. doi:10.1007/s004100000156

Nimis, P., Preston, R., Perritt, S. H., and Chinn, I. L. (2020). Diamond's depth distribution systematics. *Lithos* 376-377, 105729. doi:10.1016/j.lithos.2020.105729

Pearson, D. G., Brenker, F. E., Nestola, F., McNeill, J., Nasdala, L., Hutchison, M. T., et al. (2014). Hydrous mantle transition zone indicated by ringwoodite included within diamond. *Nature* 507, 221–224. doi:10.1038/nature13080

Potapkin, V., Chumakov, A. I., Smirnov, G. V., Celse, J. P., Rüffer, R., McCammon, C., et al. (2012). The ^{57}Fe synchrotron mössbauer source at the ESRF. *J. Synchrotron Rad.* 19 (4), 559–569. doi:10.1107/S0909049512015579

Prescher, C., and Prakapenka, V. B. (2015). DIOPTAS: a program for reduction of two-dimensional X-ray diffraction data and data exploration. *High Press. Res.* 35, 223–230. doi:10.1080/08957959.2015.1059835

Prescher, C., McCammon, C., and Dubrovinsky, L. (2012). *MossA*: a program for analyzing energy-domain mössbauer spectra from conventional and synchrotron sources. *J. Appl. Crystallogr.* 45, 329–331. doi:10.1107/S0021889812004979

Prince, E. (2004). *International tables for crystallography, volume C: mathematical, physical and chemical tables*. Springer Science and Business Media.

Purwin, H., Lauterbach, S., Brey, G. P., Woodland, A. B., and Kleebe, H. J. (2013). An experimental study of the Fe oxidation states in garnet and clinopyroxene as a function of temperature in the system CaO-FeO-Fe_2O_3-MgO-Al_2O_3-SiO_2: implications for garnet–clinopyroxene geothermometry. *Contrib. Mineral. Petrol.* 165, 623–639. doi:10.1007/s00410-012-0827-4

Quirt, D. H. (2004). Cr-diopside (clinopyroxene) as a kimberlite indicator mineral for diamond exploration in glaciated terrains. Summary of investigations 2004. *Ind. Resour. Misc. Rep*. Vol. 2 10-14.

Rüffer, R., and Chumakov, A. I. (1996). Nuclear resonance beamline at ESRF. *Hyperfine Interact.* 97, 589–604. doi:10.1007/BF02150199

Schwab, R. G., and Küstner, D. (1977). Präzisionsgitterkonstantenbestimmung zur Festlegung röntgenographischer Bestimmungskurven für synthetische Olivine der Mischkristallreihe Forsterit-Fayalit. Neues Jahrbuch für Mineralogie. *Monatshefte* 5, 205–215.

Sheldrick, G. M. (2015). Crystal structure refinement with SHELXL. *Acta Crystallogr. Sect. C. Struct. Chem.* 71 (1), 3–8. doi:10.1107/S2053229614024218

Sobolev, N. V., Lavrent'ev, Y. G., Pokhilenko, N. P., and Usova, L. V. (1973). Chrome-rich garnets from the Kimberlites of yakutia and their parageneses. *Contrib. Mineral. Petrol.* 40, 39–52. doi:10.1007/BF00371762

Sobolev, N. V., Pokhilenko, N. P., Lavrent'ev, Y. G., and Yefimova, E. S. (1977). Deep-seated xenoliths, xenocrysts in Kimberlites and crystalline inclusions in diamonds from udachnaya kimberlite pipe, yakutia. *Int. Kimberl. Conf.* 2, 328–330. doi:10.29173/ikc1038

Sobolev, N. V., Fursenko, B. A., Goryainov, S. V., Shu, J., Hemley, R. J., Mao, H., et al. (2000). Fossilized high pressure from the earth's deep interior: the coesite-in-diamond barometer. *Proc. Natl. Acad. Sci. U.S.A.* 97 (22), 11875–11879. doi:10.1073/pnas.220408697

Sobolev, N. V., Logvinova, A. M., Zedgenizov, D. A., Seryotkin, Y. V., Yefimova, E. S., Floss, C., et al. (2004). Mineral inclusions in microdiamonds and macrodiamonds from kimberlites of yakutia: a comparative study. *Lithos* 77, 225–242. doi:10.1016/j.lithos.2004.04.001

Stachel, T., and Harris, J. W. (1997). Diamond precipitation and mantle metasomatism–evidence from the trace element chemistry of silicate inclusions in diamonds from akwatia, Ghana. *Contributions Mineralogy Petrology* 129 (2), 143–154. doi:10.1007/s004100050328

Stachel, T., and Harris, J. W. (2008). The origin of cratonic Diamonds—Constraints from mineral inclusions. *Ore Geol. Rev.* 34 (1-2), 5–32. doi:10.1016/j.oregeorev.2007.05.002

Stachel, T., Banas, A., Aulbach, S., Smit, K. V., Wescott, P., Chinn, I. L., et al. (2018). The victor mine (superior craton, Canada): neoproterozoic lherzolitic diamonds from a thermally-modified cratonic root. *Mineralogy Petrology* 112, 325–336. doi:10.1007/s00710-018-0574-y

Stachel, T., Aulbach, S., and Harris, J. W. (2022). Mineral inclusions in lithospheric diamonds. *Rev. Mineralogy Geochem.* 88, 307–391. doi:10.2138/rmg.2022.88.06

Stagno, V., and Fei, Y. (2020). The redox boundaries of Earth's interior. *Elements* 16 (3), 167–172. doi:10.2138/gselements.16.3.167

Stagno, V., and Frost, D. J. (2010). Carbon speciation in the asthenosphere: experimental measurements of the redox conditions at which carbonate-bearing melts coexist with graphite or diamond in peridotite assemblages. *Earth Planet. Sci. Lett.* 300 (1-2), 72–84. doi:10.1016/j.epsl.2010.09.038

Stagno, V., Frost, D. J., McCammon, C. A., Mohseni, H., and Fei, Y. (2015). The oxygen fugacity at which graphite or diamond forms from carbonate-bearing melts in eclogitic rocks. *Contrib. Mineral. Petrol.* 169, 16. doi:10.1007/s00410-015-1111-1

Sutton, S. R., Rivers, M. L., Chariton, S., Eng, P. J., Lanzirotti, A., Newville, M., et al. (2022). GeoSoilEnviroCARS (sector 13) at the advanced photon source: a comprehensive synchrotron radiation facility for Earth science research at ambient and extreme conditions. *Phys. Chem. Minerals* 49, 32. doi:10.1007/s00269-022-01207-4

Timmerman, S., Stachel, T., Koornneef, J. M., Smit, K. V., Harlou, R., Nowell, G. M., et al. (2023). Sublithospheric diamond ages and the supercontinent cycle. *Nature* 623, 752–756. doi:10.1038/s41586-023-06662-9

Tschauner, O., Huang, S., Yang, S., Humayun, M., Liu, W., Gilbert Corder, S. N., et al. (2021). Discovery of davemaoite, $CaSiO_3$-perovskite, as a mineral from the lower mantle. *Science* 374, 891–894. doi:10.1126/science.abl8568

Ulmer, P., and Stalder, R. (2001). The Mg(Fe)SiO3 orthoenstatite-clinoenstatite transitions at high pressures and temperatures determined by raman-spectroscopy on quenched samples. *Am. Mineralogist* 86 (10), 1267–1274. doi:10.2138/am-2001-1014

Viljoen, K. S., Harris, J. W., Ivanic, T., Richardson, S. H., and Gray, K. (2014). Trace element chemistry of peridotitic garnets in diamonds from the premier (cullinan) and finsch kimberlites, South Africa: contrasting styles of mantle metasomatism. *Lithos* 208-209, 1–15. doi:10.1016/j.lithos.2014.08.010

Wallace, M. E., and Green, D. H. (1988). An experimental determination of primary carbonatite magma composition. *Nature* 335, 343–346. doi:10.1038/335343a0

Wang, W., and Gasparik, T. (2001). Metasomatic clinopyroxene inclusions in diamonds from the Liaoning Province, China. *Geochimica Cosmochimica Acta* 65 (4), 611–620. doi:10.1016/S0016-7037(00)00553-6

Wang, J., Xiong, X., Takahashi, E., Zhang, L., Li, L., and Liu, X. (2019). Oxidation state of arc mantle revealed by partitioning of V, Sc, and Ti between mantle minerals

and basaltic melts. *J. Geophys. Res. Solid Earth* 124, 4617–4638. doi:10.1029/2018JB016731

Wang, X., Zhang, J., Wang, C., Zong, K., and Xu, H. (2022). Experimental constraint on Ca-rich carbonatite melt-peridotite interaction and implications for lithospheric mantle modification beneath the north China craton. *J. Geophys. Res. Solid Earth* 127, e2022JB024769. doi:10.1029/2022jb024769

Wang, Y., Nestola, F., Li, H., Hou, Z., Pamato, M. G., Novella, D., et al. (2023). *In situ* single-crystal X-ray diffraction of olivine inclusion in diamond from Shandong, China: implications for the depth of diamond formation. *Eur. J. Mineral.* 35, 361–372. doi:10.5194/ejm-35-361-2023

Woodland, A. B., Kornprobst, J., and Tabit, A. (2006). Ferric iron in orogenic lherzolite massifs and controls of oxygen fugacity in the upper mantle. *Lithos* 89 (1-2), 222–241. doi:10.1016/j.lithos.2005.12.014

Yasuzuka, T., Ishibashi, H., Arakawa, M., Yamamoto, J., and Kagi, H. (2009). Simultaneous determination of mg# and residual pressure in olivine using micro-raman spectroscopy. *J. Mineralogical Petrological Sci.* 104 (6), 395–400. doi:10.2465/jmps.090615

Yaxley, G. M., Green, D. H., and Kamenetsky, V. (1998). Carbonatite metasomatism in the southeastern Australian lithosphere. *J. Petrology* 39 (11-12), 1917–1930. doi:10.1093/petroj/39.11-12.1917